Journal of Materials Chemistry A

Accepted Manuscript

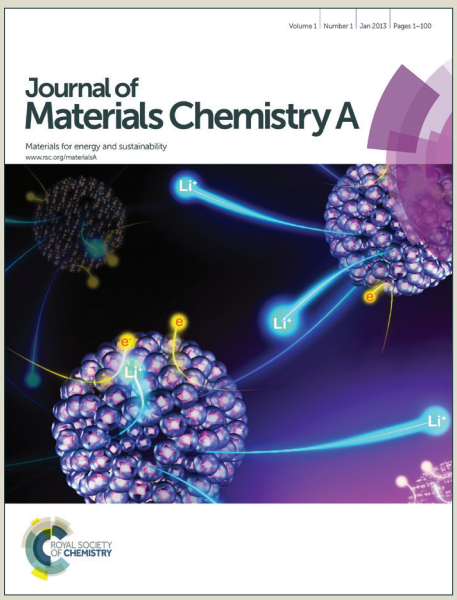

ROYAL SOCIETY OF CHEMISTRY

www.rsc.org/materialsA

Ultra-long Magnetic Nanochains for Highly Efficient Arsenic Removal from Water

Gautom Kumar Das,[a] Cecile S. Bonifacio,[b] Julius De Rojas,[c] Kai Liu,[c] Klaus van Benthem[b] and Ian M. Kennedy[a*]

Table of contents entry

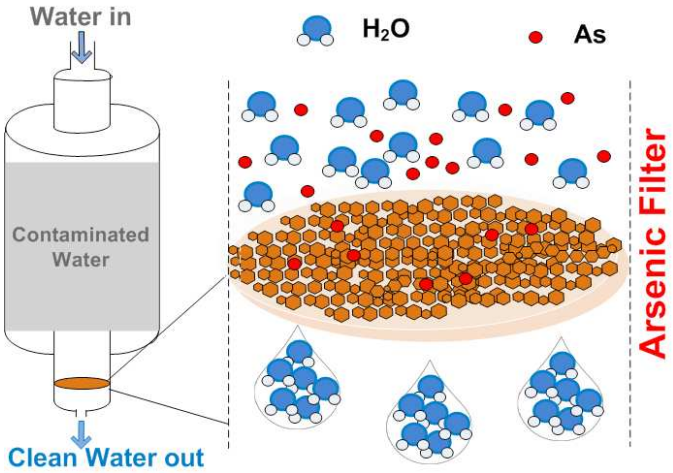

Abstract

The contamination of drinking water with naturally occurring arsenic is a global health threat. Filters that are packed with adsorbent media with a high affinity for arsenic have been used to de-contaminate water — generally iron or aluminium oxides are favored materials. Recently, nanoparticles have been introduced as adsorbent media due to their superior efficiency compared to their bulk counter-parts. An efficient nanoadsorbent should ideally possess high surface area, be easy to synthesize, and most importantly offer a high arsenic removal capacity. Achieving all the key features in a single step synthesis is an engineering challenge. We have successfully engineered such a material in the form of nanochains synthesized via a one step flame synthesis. The ultra-long γ-Fe_2O_3 nanochains possess high surface area (151.12 $m^2\ g^{-1}$), large saturation magnetization (77.1 emu g^{-1}) that aids in their gas phase self-assembly into long chains in an external magnetic field, along with an extraordinary arsenic removal capacity (162 $mg.g^{-1}$). A filter made with this material exhibited a relatively low-pressure drop and very little break-through of the iron oxide across the filter.

INTRODUCTION

Arsenic-contaminated drinking water is a serious global health concern due to its high toxicity and carcinogenicity.[1-5] The contamination in drinking water sources is estimated to affect over 144 million people around the world,[6, 7] spurring the development of numerous water treatment technologies to limit negative health impacts associated with exposure to arsenic contaminated water including cancer, skin lesions, and neurological disorders. These technologies include ion exchange, adsorptive media filtration, coagulation and flocculation, electrocoagulation, and anaerobic removal with iron sulfides. Adsorptive media filtration has been one of the most attractive approaches amongst the extant technologies due to its low cost, high efficiency, ease of processing and versatility for different water streams.[2, 3, 5, 7-9]

Inorganic arsenic is the predominant form of arsenic found in natural waters; it is found in two different oxidation states: As (III) and As (V). It was classified as the number one toxin in the U.S. Environmental Protection Agency (USEPA) list of prioritized pollutants.[10] As (III) shows higher mobility in soils and higher toxicity compared to As (V). However, pentavalent As (V) is stable in oxygen-rich aerobic environments and thus it is the predominant arsenic species under oxidizing environments. Pentavalent arsenic is therefore generally found more frequently than the trivalent form in seawater, lakes and rivers.[10] There has been a growing effort worldwide to develop efficient materials to remove arsenic from water sources to meet the maximum allowable limit in drinking water (i.e. 10 $\mu g\ L^{-1}$) set by the world health organization (WHO).

Nano-adsorbents offer significant improvements over conventional adsorbents due to their extremely high mass specific surface area, short inter-particle diffusion distance, and tunable size and surface chemistry.[11-13] A high specific surface area is mainly responsible for their high

adsorption capacity. In addition, the large surface energy and size dependent surface structure, at the nanoscale, may create highly active adsorption sites, resulting in higher adsorption capacity per unit surface area.[14, 15] One of the major limitations of using nano-adsorbents is difficulty in their application to flow-through systems. Due to their nanoscale size, they can be released from the filter or are difficult to separate, hence causing secondary pollution. To address this problem, there has been considerable effort to use support materials such as carbon, carbon nanotubes, graphene, and porous materials to contain the nano-adsorbents.[3, 4, 16] However, fabrication of such complex-structured materials can be difficult, not economical, time consuming, and often can suffer from a low mass loading of the nano-adsorbents. Therefore, an easy to synthesize, high surface area material with magnetic properties to aid in separation and assembly of structures is highly desirable in the treatment of arsenic-contaminated drinking water.

We report the one-step synthesis of high surface area (151.12 m^2g^{-1}), highly magnetic (77.1 $emug^{-1}$), ultra long γ-Fe_2O_3 nanochains (> 100 μm) decorated with ultra-small (~4 nm) γ-Fe_2O_3 nanoparticles. Iron oxide has a high adsorption capacity and excellent selectivity for arsenic.[17] Our magnetic chains with a heterogeneous surface were prepared in a facile, controllable flame synthesis under a magnetic field. The nanochains were demonstrated in a flow-through water filtration system (Scheme 1), which showed an extraordinary arsenic removal capacity (162 mg g^{-1}) with low-pressure drop and very little break-through of the iron oxide.

Experimental Section

Chemicals. All chemicals were analytical grade and used as received without further purification. Iron pentacarbonyl ($Fe(CO)_5$, AlfaAesar, 99.5%) was chosen as the iron precursor. Compressed H_2 gas was supplied from Praxair Inc. (San Ramon, CA) with stated purity of 99.5% or higher.

For As (V) adsorption isotherm experiments, As (V) stock solutions were prepared from reagent grade $Na_2HAsO_4 \cdot 7H_2O$ (AlfaAesar) in deionized water (MilliQ, Millipore Corp., Billerica, MA). The ionic strength of the test solution was adjusted using sodium nitrate ($NaNO_3$, Sigma Aldrich). HEPES sodium salt (Fisher Scientific) used as a buffer at pH 7. 70% HNO_3 (trace metal grade concentrated nitric acid, Optima, Fisher Scientific) was used to digest the sample for analysis by inductively coupled plasma mass spectrometry (ICP-MS).

Synthesis of High Surface Area Magnetic Nanochains. The magnetic nanochains were synthesized in a H_2/air diffusion flame as previously reported by our group with some modification.[18, 19] H_2 was bubbled though the liquid $Fe(CO)_5$ precursor at room temperature at a rate of 0.12 liter min^{-1} and the precursor-laden H_2 stream was passed through the central annulus in a co-annular burner (Figure 1). HEPA filtered, particle-free air was co-flowed though the outermost honeycomb annulus of the burner at a speed of ~2.2 m s^{-1} which maintain a uniform laminar flow in the working section. An additional H_2 gas stream (0.25 liter min^{-1}) was flown though the middle annulus of the burner to dilute the precursor-laden H_2 stream (a 4-channel MKS 647C (MKS Instrument Inc., MA) mass flow controller was used to control all flow rates). The concentration of $Fe(CO)_5$ in the fuel gas was estimated from the mixing ratio of the Fe-laden H_2 and pure H_2, assuming that the carrier gas was saturated with $Fe(CO)_5$ vapor.

A stable, self-sustaining laminar diffusion flame (height ~50 mm) was established on the tubular burner that generated the iron oxide nanoparticles. A homogeneous magnetic field was established by placing two 300 mm tall stacks of magnetic bars (Rare Earth Neodymium Magnets, dimension: 25 × 6 × 6 mm) on each side of the flow, parallel to each other with a spacing of 10-20 mm. The magnets were as tall as the exhaust stream of the flame gas and particles before it entered to the filter housing for collection. Iron oxide nanoparticles were

generated as individual particles in the flame; however, under the magnetic field they aligned and assembled in to ultra-long nanochains. The chains were then collected on filter paper (Whatman® qualitative filter paper, Grade 1, Sigma-Aldrich) in a system consisting of a funnel that was mounted co-axially with the flame, a filter housing, and a vacuum system.

Characterization. The flame-synthesized iron oxide nanochains were characterized by a FEI/Philips XL-30 Field Emission Scanning Electron Microscope (SEM) operated at 5 kV. Transmission Electron Microscopy (TEM) images were acquired using a Phillips CM-12 TEM operating at 120 kV. Higher resolution TEM experiments were carried out with an aberration-corrected JEOL JEM 2100F/Cs scanning transmission electron microscope (STEM) operated at 200 kV. Electron energy loss spectroscopy (EELS) data of the Fe $L_{2,3}$ absorption edges were recorded with a Gatan Tridiem parallel electron energy-loss spectrometer that is attached to the JEOL JEM 2100F/Cs instrument. Crystallinity was identified using a Scintag powder X-ray diffractometer (XRD) with Cu *K*α radiation operated at 45 kV and 40 mA. The powder was scanned for 2θ = 20°- 70°. The scanning step size was 0.015° in 2θ with a counting time of 1 s per step. Brunauer–Emmett–Teller (BET) surface area measurements were carried out using N_2 gas adsorption in an AUTOSORB-1 using an optimized protocol (Quantachrome Instruments, Boynton Beach, FL, USA). The samples were de-gassed at 120 °C for 24 h prior to the adsorption-desorption cycle. The magnetic characterization of the nanochains was carried out with a Princeton Measurements Corp. 3900 vibrating sample magnetometer (VSM). The measurements were carried out on powdered samples, with chains oriented randomly in the magnetic field. Arsenic concentrations were analyzed using ICP-MS (7500i, Agilent Technologies, Wilmington, DE, USA).

Arsenic Adsorption Test. Arsenic adsorption isotherms were acquired separately in flow-through and batch experiments. Arsenic adsorption kinetics were determined in a batch experiment by mixing 20 mg of iron oxide nanochains with 10 ml of arsenic water with a concentration of 100 mg L^{-1}. The suspension was placed in a rotary shaker with a speed of 200 rpm at room temperature for 3 h. The nanoparticle adsorbents were then separated by centrifugation and the liquid collected for analysis. For the flow-through filtration experiments, 200 ml of water containing arsenic of different concentrations (ranging from 0.25 to 300 mg L^{-1}) was filtered though a filter paper (Whatman® qualitative filter paper, Grade 1, Sigma-Aldrich) with a uniformly covered layer of 20 mg iron oxide nano-chains as shown in Figure S1. The flow rate of the liquid was determined (from the batch experiment) to maintain a fixed contact time of 90 min in all the experiments. The filtered water was collected for analysis. All the experiments were conducted at pH 7.0. The solution pH was maintained using 1 mM HEPES. All the treated water collected after filtration and centrifugation was dissolved in 70% HNO_3 and analyzed in ICP-MS. The equilibrium-sorption capacity (Q_e) was calculated from the following equation:[20]

$$Q_e = (C_0 - C_v)V/m \quad (1)$$

C_0 and C_v represent the concentration of As(V) before and after removal, respectively. *V* is the volume of the solution and *m* is the mass of the adsorbent.

The Langmuir model was used to fit the experimental data according to the following equation:

$$Q_e = Q_{max}\, b\, C_e/(1+bC_e) \quad (2)$$

where Q_e is the adsorption capacity of the adsorbent (γ-Fe_2O_3 nanochains) at equilibrium. C_e is the equilibrium concentration of arsenic in the solution, Q_{max} is the saturation adsorption capacity of the γ-Fe_2O_3 nanochains, and b is the Langmuir equilibrium constant.

Results and Discussion

The flame synthesis produced very long nanochains as shown in the SEM image of Figure 2 and Figure S2. The chains consisted of individual nanoparticles (~ 50 nm) that self-assembled into structures that were several hundred microns long with an aspect ratio in the order of 10^3 - 10^4. Ultra-small nanoparticles were also present and were associated with the 50 nm primary nanoparticles – they were not visible in the SEM image. Therefore, transmission electron micrographs were taken. The high resolution TEM micrograph in Figure 3a shows a small part of the long nanochains which are covered with ultrasmall (~ 4 nm) nanoparticles and dangling clusters of ultrasmall nanoparticles. A high angle annular dark field (HAADF) STEM image was taken (see Figure 3b) as a survey image for subsequent EELS experiments.. The HAADF STEM image confirms the presence of the ultrasmall nanoparticles that decorate the surface of the nanoparticles. EELS measurements of the O K and Fe $L_{2,3}$ absorption edges were carried out from a number of different individual nanoparticles (Figure 4). The near-edge fine structure of the O K edge shown in Figure 4a is excellent agreement with previously reported studies of γ-Fe_3O_4.[21] The acquired Fe L_3 and L_2 edges were subsequently fitted, after background subtraction, by either a single or two Gaussian peaks whichever yielded the best quality fit. The L_3/L_2 intensity ratio was determined by the ratio of the integrated areas beneath the absorption edges. The observed L_3/L_2 intensity ratio of 5.50 ± 0.04 is in excellent agreement with previously

reported data for Fe^{III+} in γ-Fe_2O_3 hence confirming that the nanochains are formed from γ-Fe_2O_3 nanoparticles.[22-24]

The BET method was used to obtain the surface area of the chains. Figure S3a shows that the BET surface area was 151 $m^2 g^{-1}$. In a study with similar nanoparticles synthesized in the gas phase, Guo et al. [18] showed that about 80% of the surface area was accounted for by the small particles. Therefore, we believe that the high surface area obtained for the nanochains is mainly due to the large coverage of the ultra-small nanoparticles on the nanochains. The large surface area can offer a great advantage for efficient arsenic removal.

The crystallinity of the nanochains was analyzed by powder XRD. The XRD pattern (Figure S3b) showed that the crystalline phase of the nanochains was γ-Fe_2O_3 (PDF # 39-1346) which is in perfect agreement with the EELS data. Magnetic properties of the particles were analyzed by VSM. The room temperature M-H hysteresis loop of the nanochains (Figure 5) shows a saturation magnetization of 77 emu g^{-1}, consistent with bulk value.[25] The coercivity is 290 Oe, enhanced over typical values in bulk materials due to the finite size of the nanoparticles.[26-28] The large magnetization with modest coercivity is highly desirable for many practical applications so that a strong magnetic response can be obtained at a low applied magnetic field.

To understand the mechanism of the formation of the nanochains, samples were taken from different points in the flame and in the exhaust stream. The flame was about 50 mm long. Aerosol samples were collected thermophoretically and examined by TEM. We found most of the nanoparticles formed between the mid-flame region to the flame tip, in a reducing environment. A typical TEM image taken at the visible tip of the flame is shown in Figure S4. Both ultra-small nanoparticles and primary nanoparticles formed at this point, but they had not

formed long chains. The observed results are in good agreement with the previous studies.[18, 29] From the mid-flame zone, nanoparticles started to form due to reduction of the iron precursor $Fe(CO)_5$ followed by oxidation closer to the reaction zone where OH can be present.[29] As per our observation, nanochain formation took place mostly in the exhaust stream under the magnetic field, growing longer with greater retention time as they were transported by the flow. Based on our observation and the literature data,[18, 29-31] we propose a formation mechanism of chains under such magnetic field. The mechanism is schematically shown in the Figure 1.

First, deep on the fuel side of the flame, the precursor $Fe(CO)_5$ pyrolyzed into elemental Fe and CO. As Fe moves along the flame axis, Fe oxidizes to FeO due to increased temperature and oxidizer concentrations (primarily OH with some O). Then in the maximum temperature reaction region in the flame, some of the condensed phase FeO converts to vapor FeO. The majority of the FeO is oxidized in the reaction zone to crystalize into 50 nm particles. In the post-flame region, the Fe and FeO vapor nucleate to form very small particles that are transformed to γ-Fe_2O_3 due to super-stoichoimetric oxygen – these ultra-small particles are scavenged by the larger particles. Up to the point of the visible tip of the flame, there was no substantial difference in particle assembly or chain formation with or without a magnetic field (Figure S5). However, in the post-flame zone, nanoparticles self-assembled and aligned as long nanochains under a magnetic field as shown in the Figure 2. At the center-line of the flow, the magnetic flux was measured to be 350 mT with a 5180 Hall Effect/Tesla Meter with a resolution of 100 μT. Interestingly, in the absence of a magnetic field, chains were still formed but in the form of fractal aggregates[32, 33] (Figure S6).

Deposition on cooled metal surfaces, produced by thermophoresis, resulted in branch random aggregation of nanoparticles. This kind of fractal aggregate has been reported for other oxide-

based nanoparticle aggregates and supported by theoretical understanding of nanoparticle formation and aggregation.[32-36] In the absence of a magnetic field, the magnetization directions of the particles are random and dipole interactions amongst them could be either magnetizing or demagnetizing.[37] Overall the interaction among the adjacent particles favors bridging and inter-connection which result in fractal aggregates. However, an external magnetic field in a gas phase process strongly influenced the alignment and the growth mechanism of nanoparticles. The 350 mT magnetic field along the flow path was three order of magnitude larger than the particle coercivity and fully saturates the particles in the single domain state. These particles then preferentially aligned along the field direction where the dipole interactions were magnetizing,[37] favoring linear chain growth along the magnetic-field flux lines,[38] and leading to the formation of long straight chains.[39, 40] The as-formed particle-chains strongly enhanced the local magnetic field and rapidly attracted the nearby ultra-small magnetic nanoparticles, which ultimately resulted in efficient scavenging of the smaller aerosol mode and the formation of decorated long magnetic chains. In fact, the large ferromagnetic nanoparticles could independently attract and attach the ultra-small superparamagnetic nanoparticles. The creation of the two co-located size modes is a key advantage of using this technique to generate nanochains with a large surface area without a tedious multi-step processes.

The heterogeneous surface of the nanochains with large specific surface area and large magnetization make them very promising for application to the removal of arsenic from water. We started testing this material by looking at the adsorption kinetics of the nanochains. The time course of the adsorption of the As (V) by the γ-Fe_2O_3 nanochains is shown in Figure 6. It can be seen that the first 15 min corresponded to a rapid adsorption stage. Thereafter, the adsorption rate decreased and equilibrium was reached in about 45 min. The residual concentration at

equilibrium was found to be 16.1 mg L^{-1} from an initial concentration of 100 mg L^{-1}. The adsorption kinetics indicated that the adsorption of As(V) occurred on the surface of the nanochains rapidly, which we attributed to the surface-bound ultra-small particles and the associated heterogeneity. Thereafter, the adsorbent sites on the particle surface competed with the rest of the ions, giving rise to low adsorption rates. In comparison to other adsorbents reported in the literature, the γ-Fe_2O_3 nanochains showed very high adsorption rates. For example, bioadsorpbents[41, 42] required several hours to reach equilibrium, activated alumina[43] required about 2 days. However, the quick adsorption of our nanochains was accomplished in about 30 - 45 min, which offers promise in practical applications such as a flow-through filter system.

The adsorption isotherm of the nanochains was determined for the flow-through filter system for different concentrations of arsenic in water (0.25 to 300 mg. L^{-1}). The amount of As(V) that was adsorbed on the γ-Fe_2O_3 nanochains at equilibrium (Q_e) increased with increasing C_e. In our experimental range, the maximum C_e we obtained was 141 mg L^{-1}. The isotherm between Q_e vs C_e is presented in Figure 7. As seen in the figure, the nanochains showed an excellent maximum adsorption capacity which was calculated to be 162 mg L^{-1}. A comparison of our chains with other reported or available materials is presented in Table 1. Generally, a large specific surface area (S_{BET}) is primarily responsible for the strong adsorption behavior of metal oxides. However, as seen in the Table 1, nanoparticles possessing similar or higher S_{BET} showed different adsorption capacity, which suggest that mass specific surface area may not be the only determining factor for high adsorption capacity. According to previous reports, the other critical factor is the presence of active sites on the adsorbents that is influenced by the synthesis methods. Previous studies showed that the removal of arsenic from aqueous solution by iron oxides or hydroxides depends on active sites such as surface density of hydroxyl groups (-OH), which can

form complexes with arsenic ions.[44-46] The ultra-small nanoparticles decorated on the long nanochains created a heterogeneous surface which generated more active sites than a homogeneous surface of similar size and specific surface area. The abundance of active sites is thus believed to be primarily responsible for such high adsorption capacity. To understand the type of adsorption, a Langmuir adsorption isotherm were fitted to the experimental data points. The details of the Langmuir parameters are summarized in the Figure 7. The maximum adsorption constant obtained for the Langmuir model is 162 mg g^{-1}. As we can see, the fitted curve matches very well with the Langmuir isotherm ($R^2 > 0.97$) which suggests that the adsorption of arsenates occurs mostly by monolayer formation. We note that although we did not examine the effect of pH and the impact of competitive ions on adsorption of arsenic on γ-Fe_2O_3 , these issues have been studied elsewhere[46] and have confirmed the excellent selectivity of this material for arsenic removal.

In addition to high adsorptivity, the nanochains present less pressure drop to flow compared to the constituent nanoparticles that were simply packed into a bed, probably as a result of a greater void volume. The fine spacing of the nanochains in the filter did not lead to a diffusional barrier to adsorption. The comparative pressure drop was assessed by creating filters of similarly-sized nanoparticles that were synthesized with and without applying the magnetic field. A large area SEM image of the nanoparticles deposited on the filter is shown in Figure S7. Water flowed through the filters (i.e. nanochains or deposited nanoparticles) for a given period of time. The height of the water column was maintained constant by continuously adding make-up water during the experiments in order to maintain a constant head on the filter. As shown in Figure 8, the volume of collected water using nanochains as a filter material was as much as twice that of non-chain simply aggregated nanoparticles. The low-pressure drop is a key for any filtration

system. Therefore, we believe that the nanochains offer an advantage compared to the nanoparticles in terms of handling more filtrate in a given time.

We have also examined how much iron oxide particles are released from the filter at a moderate flow condition. For this experiment, arsenic contaminated water was passing through the filter covered with (i) nanoparticle, and (ii) nanochains as adsorbent, at a rate of 0.5 L min^{-1} for a fixed total time. Equal volumes of filtered water were analyzed for both cases by ICP-MS. The result presented in Figure 8 shows that for a given mass of adsorbent material, Fe ions were detected in water at a concentration 12.7 times higher for nanoparticles compared to the nanochains (for the given dilution used in ICPMS, $Fe_{nanoparticles}$ = 660 ± 120 ppb; $Fe_{nanochains}$ = 51.9 ± 20.2 ppb). The data were obtained in three independent experiments. The result shows that the nanochains could not entirely eliminate the break-through of particles from the filter. However, the difference is significant. Complete sintering of the chains, in principle, could possibly eliminate the break-through of iron nanoparticles, through a modification of the synthesis conditions, primarily flame temperature.

Conclusion

In summary, we present a very simple strategy to produce a highly efficient material (Q_m = 162 mg g^{-1}) with a heterogeneous surface for arsenic removal. High efficiency is attributed to the ultra-small nanoparticles that decorate larger nanoparticles, along with the increase in the active sites for arsenic binding. The arsenic adsorption process obeys the Langmuir isotherm model suggesting a monolayer adsorption. The magnetically-assembled nanochains offer low pressure drop and less release of iron nanomaterial from the filter than simple aggregated nanoparticles. The high magnetism and high adsorption capacity make the nanochains an ideal magnetic

adsorbent for As(V) removal by filtration with the possibility of down-stream magnetic separation.

Acknowledgments

The project was supported by the W. M. Keck Foundation with a research grant in science and engineering. We acknowledge the support of Award Number P42ES004699 from the National Institute of Environmental Health Sciences (GKD and IMK), and DMR-1008791 from the National Science Foundation (JdR and KL). CSB and KvB acknowledge financial support through an NSF CAREER award (DMR-0955638). The content is solely the responsibility of the authors and does not necessarily represent the official views of the Keck Foundation, the National Science Foundation or the National Institute of Environmental Health Sciences. The authors would also like to thank Mr. Joel Commisso (Spectroscopist, UC Davis/Interdisciplinary Center for Plasma Mass Spectrometry) for help in ICPMS analysis and Ms. Margot Rochesani, a French visiting student, for her help in conducting experiments.

Notes and references

[a] Department of Mechanical and Aerospace Engineering
[b] Department of Chemical Engineering and Materials Science
[c] Department of Physics
One Shields Avenue, University of California, Davis, CA, 95616.
* Corresponding author Email: imkennedy@ucdavis.edu

†Electronic Supplementary Information (ESI) available: Additional text and Figures S1−S7. XRD pattern, BET surface area measurment, TEM and SEM images. See DOI: 10.1039/b000000x/

1. T. M. Clancy, K. F. Hayes and L. Raskin, *Environ. Sci. Tech.*, 2013, **47**, 10799-10812.
2. D. Mohan and C. U. Pittman Jr, *J Hazard. Mater.*, 2007, **142**, 1-53.
3. V. Chandra, J. Park, Y. Chun, J. W. Lee, I.-C. Hwang and K. S. Kim, *ACS Nano*, 2010, **4**, 3979-3986.
4. J. Yang, H. Zhang, M. Yu, I. Emmanuelawati, J. Zou, Z. Yuan and C. Yu, *Adv. Func. Mater.*, 2013, **24**, 1354-1363.
5. Z. Wu, W. Li, P. A. Webley and D. Zhao, *Adv. Mater.*, 2012, **24**, 485-491.
6. X. Qu, J. Brame, Q. Li and P. J. J. Alvarez, *Acc. Chem. Res.*, 2012, **46**, 834-843.
7. R. B. Johnston, S. Hanchett and M. H. Khan, *Nat. Geosci.*, 2010, **3**, 2-3.

8. Z. Gu, J. Fang and B. Deng, *Environ. Sci. Tech.*, 2005, **39**, 3833-3843.
9. T. Tuutijärvi, J. Lu, M. Sillanpää and G. Chen, *J Hazard. Mater.*, 2009, **166**, 1415-1420.
10. J. C. Ng, J. Wang and A. Shraim, *Chemosphere*, 2003, **52**, 1353-1359.
11. C. T. Yavuz, J. T. Mayo, W. W. Yu, A. Prakash, J. C. Falkner, S. Yean, L. Cong, H. J. Shipley, A. Kan, M. Tomson, D. Natelson and V. L. Colvin, *Science*, 2006, **314**, 964-967.
12. J. T. Mayo, C. Yavuz, S. Yean, L. Cong, H. Shipley, W. Yu, J. Falkner, A. Kan, M. Tomson and V. L. Colvin, *Sci. Technol. Adv. Mat.*, 2007, **8**, 71.
13. T. Phenrat, N. Saleh, K. Sirk, R. D. Tilton and G. V. Lowry, *Environ. Sci. Tech.*, 2006, **41**, 284-290.
14. M. Auffan, J. Rose, O. Proux, D. Borschneck, A. Masion, P. Chaurand, J.-L. Hazemann, C. Chaneac, J.-P. Jolivet, M. R. Wiesner, A. Van Geen and J.-Y. Bottero, *Langmuir*, 2008, **24**, 3215-3222.
15. S. C. Bolyard, D. R. Reinhart and S. Santra, *Environ. Sci. Tech.*, 2013, **47**, 8114-8122.
16. S. Vadahanambi, S.-H. Lee, W.-J. Kim and I.-K. Oh, *Environ. Sci. Tech.*, 2013, **47**, 10510-10517.
17. S. C. N. Tang and I. M. C. Lo, *Water Res.*, 2013, **47**, 2613-2632.
18. B. Guo and I. M. Kennedy, *Aerosol Sci. Tech.*, 2007, **41**, 944-951.
19. A. D. Abid, M. Kanematsu, T. M. Young and I. M. Kennedy, *Aerosol Sci. Tech.*, 2013, **47**, 169-176.
20. F. Mou, J. Guan, H. Ma, L. Xu and W. Shi, *ACS Appl. Mater. Inter.*, 2012, **4**, 3987-3993.
21. A. Gloter, A. Douiri, M. Tence and C. Colliex, *Ultramicroscopy*, 2003, **96**, 385-400.
22. C. Colliex, T. Manoubi and C. Ortiz, *Phys. Rev. B*, 1991, **44**, 11402-11411.
23. D. H. Pearson, B. Fultz and C. C. Ahn, *Appl. Phys. Lett.*, 1988, **53**, 1405-1407.
24. J. Jasinski, K. E. Pinkerton, I. M. Kennedy and V. J. Leppert, *Microsc. Microanal.* , 2006, **12**, 424-431.
25. B. D. Cullity and C. D. Graham, John Wiley & Sons, Inc., Hoboken, New Jersey, 2009, p. 193.
26. K. Liu and C. L. Chien, *IEEE Trans. Magn.*, 1998, **34**, 1021.
27. K. Liu, L. Zhao, P. Klavins, F. E. Osterloh and H. Hiramatsu, *J. Appl. Phys.*, 2003, **93**, 7951-7953.
28. X. Kou, X. Fan, R. K. Dumas, Q. Lu, Y. Zhang, H. Zhu, X. Zhang, K. Liu and J. Q. Xiao, *Adv. Mater.*, 2011, **23**, 1393.
29. B. Guo and I. M. Kennedy, *Aerosol Sci. Tech.*, 2004, **38**, 424-436.
30. B. K. McMillin, P. Biswas and M. R. Zachariah, *J Mater. Res.*, 1996, **11**, 1552-1561.
31. H. Wang, Y. Yu, Y. Sun and Q. Chen, *Nano*, 2011, **06**, 1-17.
32. T. T. Charalampopoulos and G. Shu, *Appl. Opt.*, 2003, **42**, 3957-3969.
33. C. M. Sorensen, *Aerosol Sci. Tech.*, 2011, **45**, 765-779.
34. C.-H. Luo, W.-M. Grace Lee, Y.-C. Lai, C.-Y. Wen and J.-J. Liaw, *Atmos. Environ.*, 2005, **39**, 3565-3572.
35. M. Lattuada, H. Wu and M. Morbidelli, *J Colloid Interf. Sci.*, 2003, **268**, 106-120.
36. T. T. Charalampopoulos and G. Shu, *Appl. Opt.*, 2002, **41**, 723-733.
37. D. A. Gilbert, G. T. Zimanyi, R. K. Dumas, M. Winklhofer, A. Gomez, N. Eibagi, J. L. Vicent and K. Liu, *Sci. Rep.*, 2014, **4**, 4204.
38. G. Cheng, D. Romero, G. T. Fraser and A. R. Hight Walker, *Langmuir*, 2005, **21**, 12055-12059.
39. Y. Lalatonne, J. Richardi and M. P. Pileni, *Nature Materials* |, 2004, **3**, 121-125.

40. F. E. Osterloh, H. Hiramatsu, R. K. Dumas and K. Liu, *Langmuir*, 2005, **21**, 9709-9713.
41. L. Chai, Y. Chen and Z. Yang, *Water Environ. Res.*, 2009, **81**, 843-848.
42. B. J. McAfee, W. D. Gould, J. C. Nadeau and A. C. A. da Costa, *Separation Science and Technology*, 2001, **36**, 3207-3222.
43. T.-F. Lin and J.-K. Wu, *Water Res.*, 2001, **35**, 2049-2057.
44. S. Fendorf, M. J. Eick, P. Grossl and D. L. Sparks, *Environ. Sci. Tech.*, 1997, **31**, 315-320.
45. X. Guo, Y. Du, F. Chen, H. S. Park and Y. Xie, *J Colloid Interf. Sci.*, 2007, **314**, 427-433.
46. S. Lin, D. Lu and Z. Liu, *Chem. Eng. J*, 2012, **211–212** 46–52.
47. B. Wang, H. Wu, L. Yu, R. Xu, T.-T. Lim and X. W. Lou, *Adv. Mater.*, 2012, **24**, 1111-1116.
48. F. Mou, J. Guan, Z. Xiao, Z. Sun, W. Shi and X.-a. Fan, *J Mater. Chem.*, 2011, **21**, 5414-5421.
49. S. Zhang, H. Niu, Y. Cai, X. Zhao and Y. Shi, *Chem. Eng. J*, 2010, **158**, 599-607.
50. M. Kanematsu, T. M. Young, K. Fukushi, D. A. Sverjensky, P. G. Green and J. L. Darby, *Environ. Sci. Tech.*, 2010, **45**, 561-568.

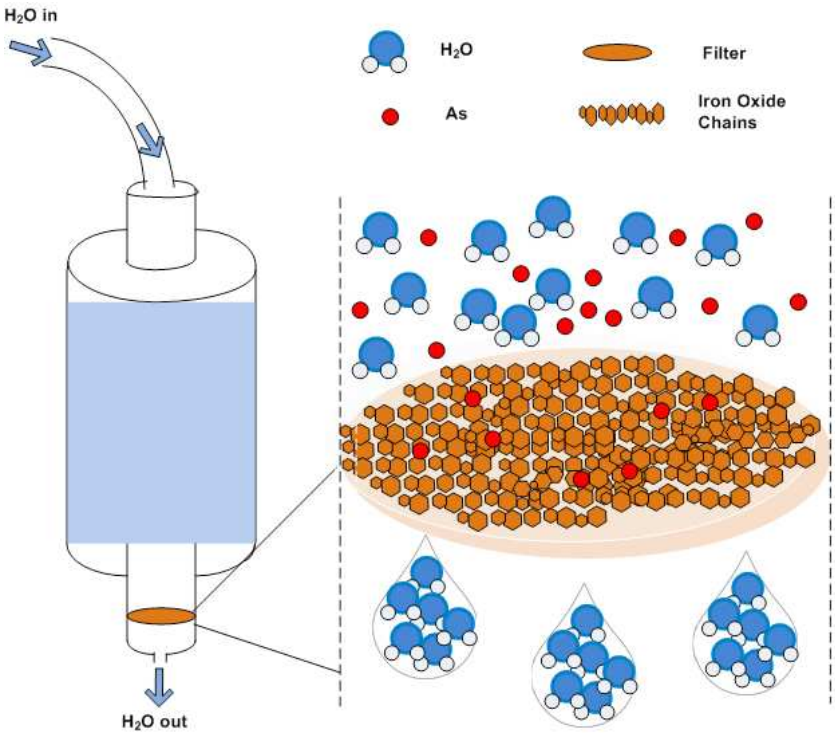

Scheme 1. Schematic of arsenic removal filtration system using a filter covered with long iron oxide nanochains.

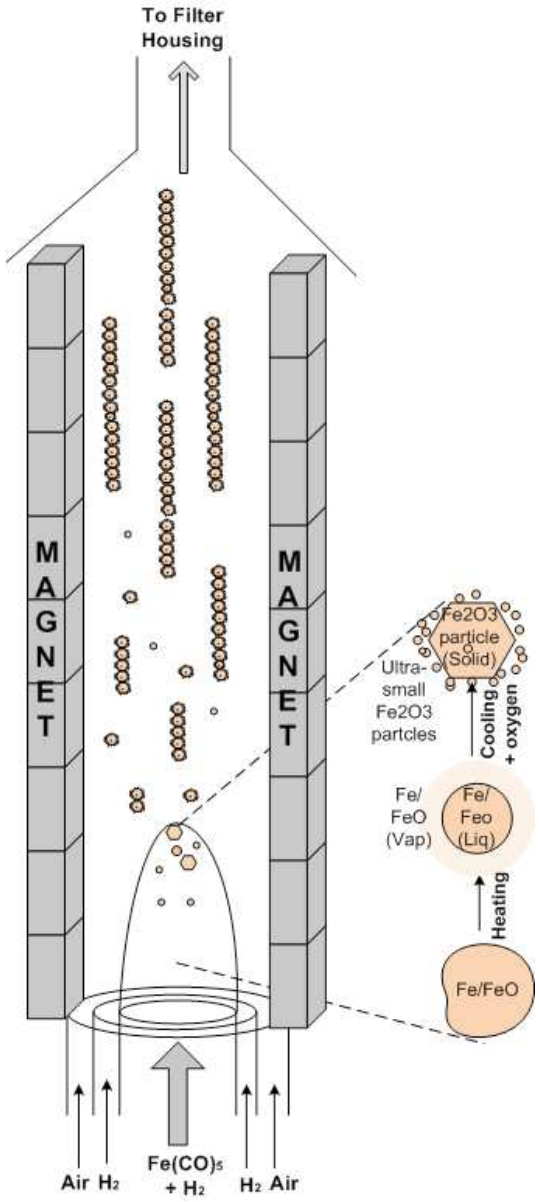

Figure 1. Flame synthesis set-up. The magnified area shows different phases of iron oxide nanoparticles formation in different flame heights.

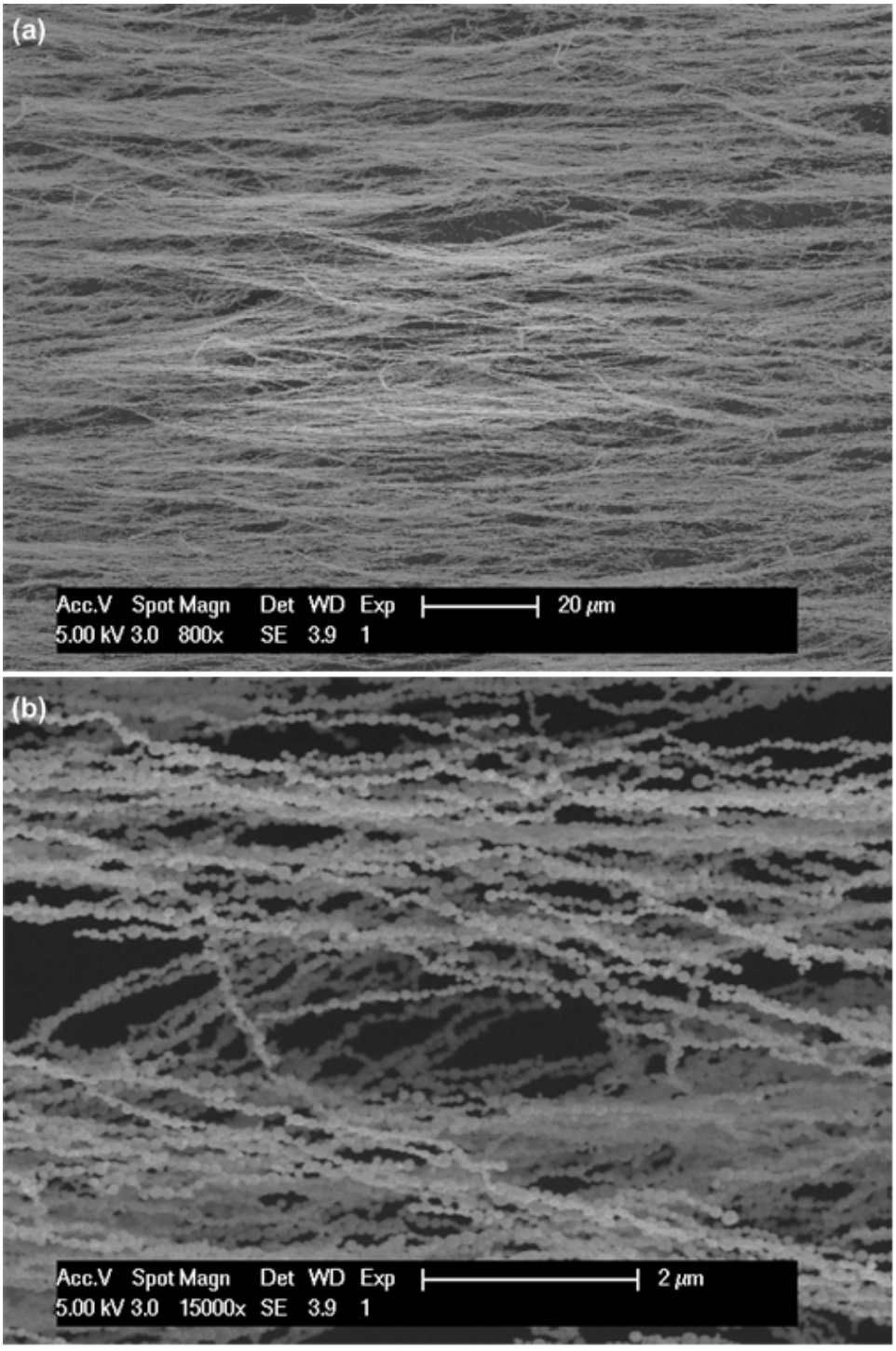

Figure 2. (a) Large area SEM images of the ultra-long nanochains of iron oxides, (b) Magnified view of the chains showing that each chain is made with thousands of nanoparticles forming a necklace-type structure.

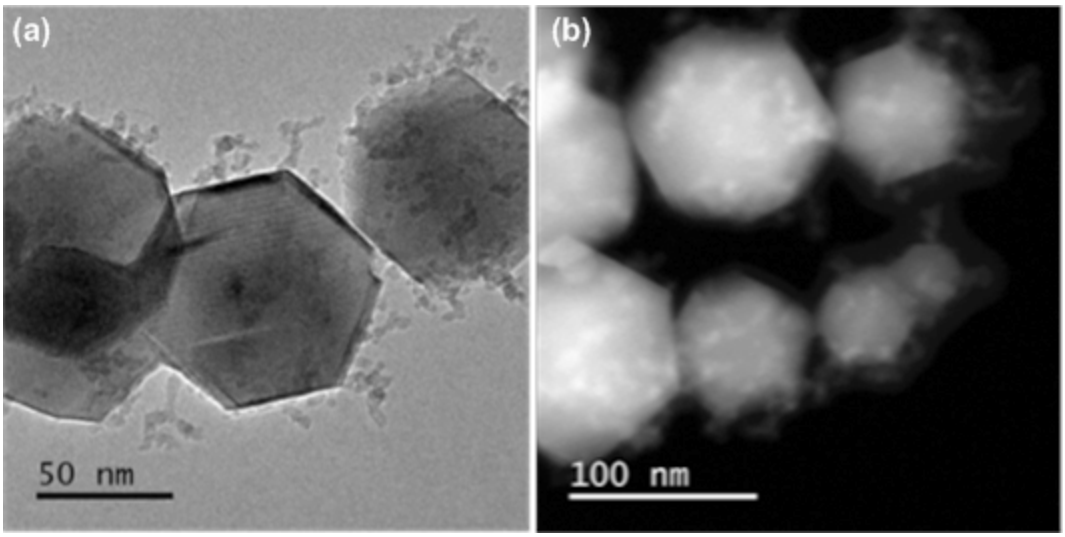

Figure 3. (a) High resolution TEM image of individual nanoparticle of the chains show that they are covered with many ultra-small particles and dangling chains/clusters. (b) Annular dark field STEM image showing the morphology of the particles as well as the texture (heterogeneity) in the surface of the nanoparticles created by ultra-small particles.

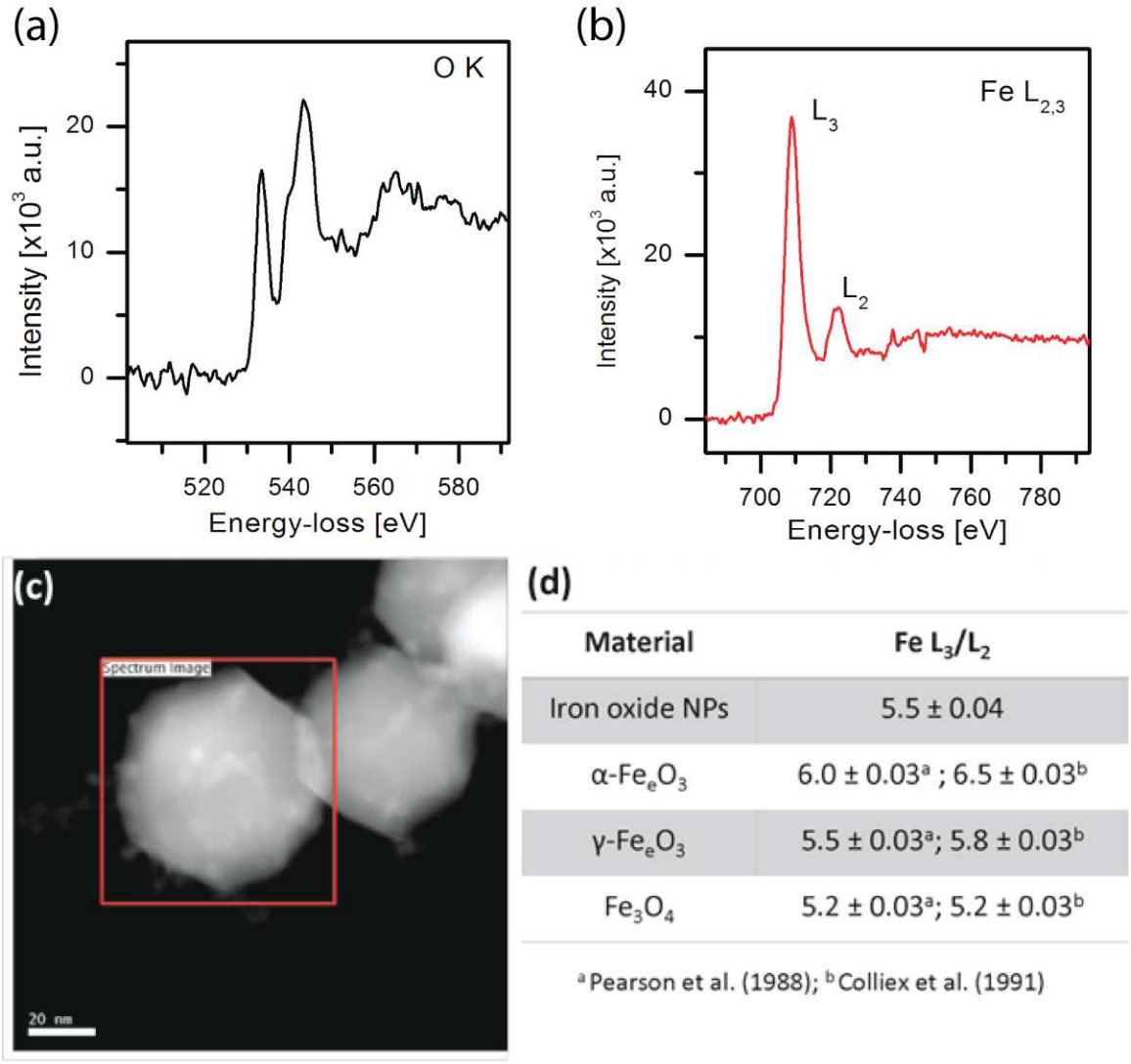

(d)

Material	Fe L_3/L_2
Iron oxide NPs	5.5 ± 0.04
α-Fe_eO_3	6.0 ± 0.03[a] ; 6.5 ± 0.03[b]
γ-Fe_eO_3	5.5 ± 0.03[a]; 5.8 ± 0.03[b]
Fe_3O_4	5.2 ± 0.03[a]; 5.2 ± 0.03[b]

[a] Pearson et al. (1988); [b] Colliex et al. (1991)

Figure 4. EELS O K (a) and Fe $L_{2,3}$ (b) ionization edges acquired from the marked area of the HAADF STEM image in (c). The calculated Fe L_3/L_2 EELS intensity ratio from (b) verified the γ-Fe_2O_3 phase of the NPs when compared with reference values from the different oxidation states of iron oxide from the literature (d).

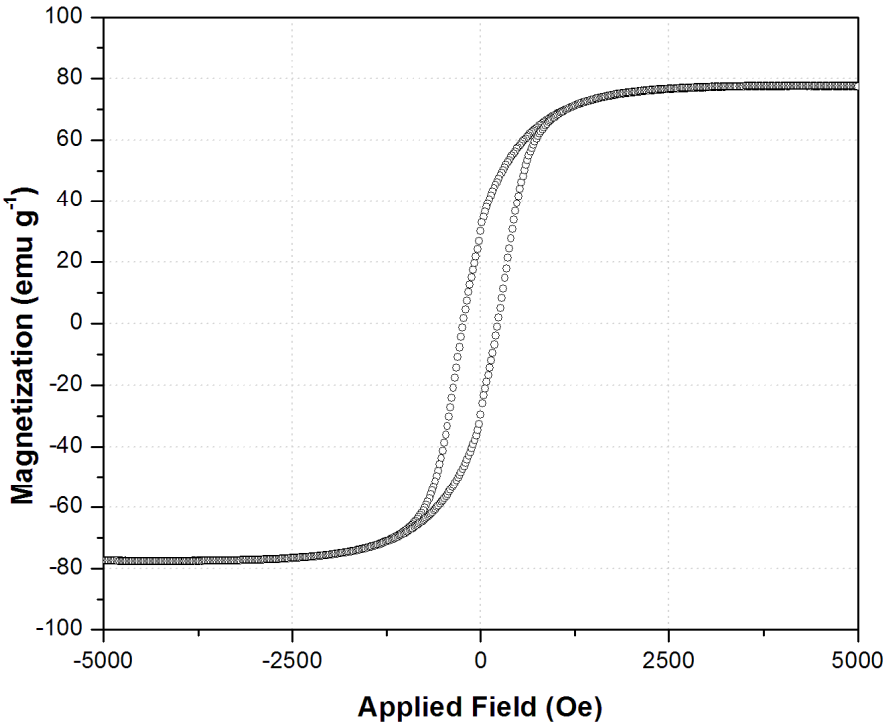

Figure 5. Room temperature magnetic hysteresis loop of the γ-Fe_2O_3 nanochains shows a saturation magnetism of 77 emu g^{-1} and coercivity of 290 Oe.

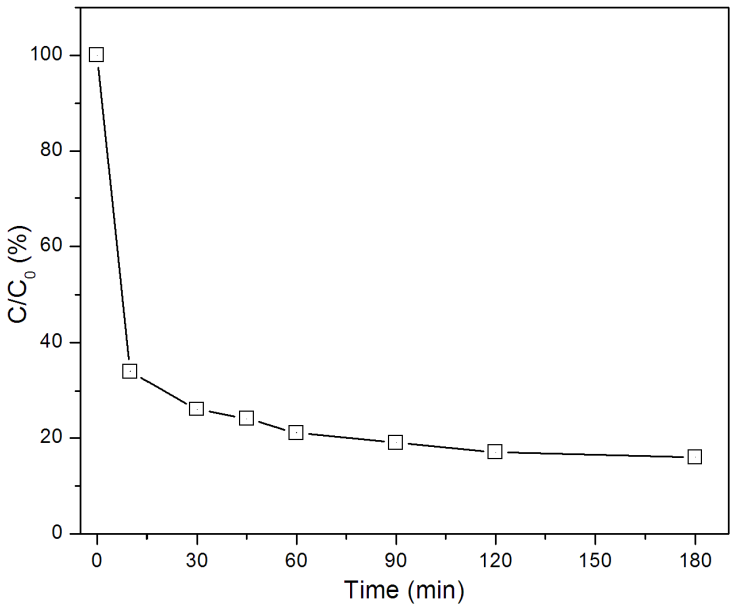

Figure 6. Kinetics of adsorption of As (V) on the γ-Fe_2O_3 nanochains at room temperature.

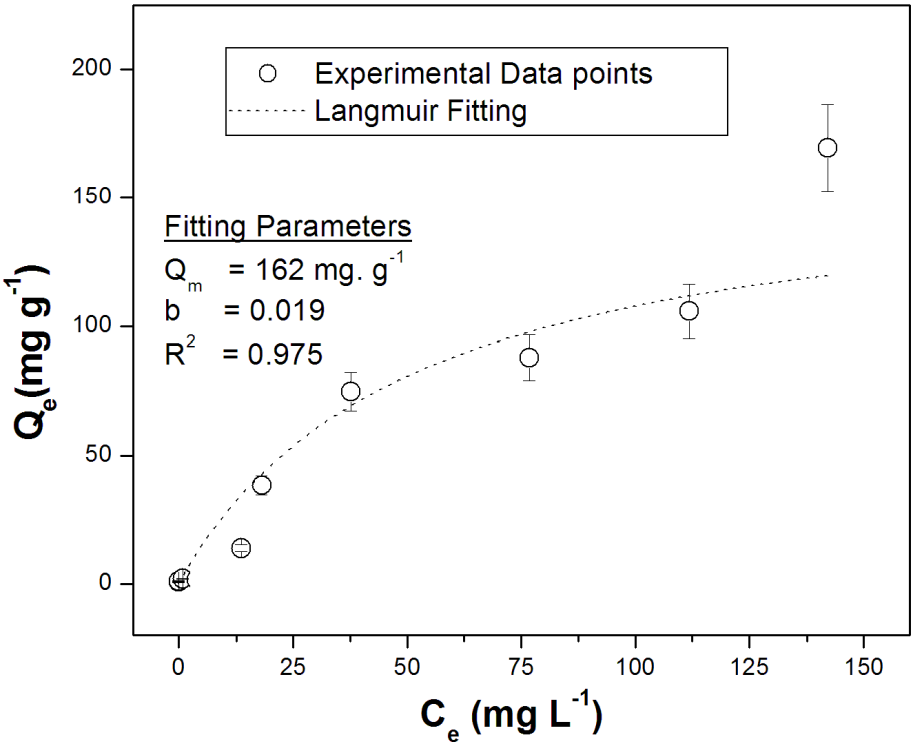

Figure 7. Room temperature equilibrium isotherm data of As (V) adsorption on the γ-Fe_2O_3 nanochains at pH = 7. Langmuir isotherm model was fit on to experimental data shown with the dotted line.

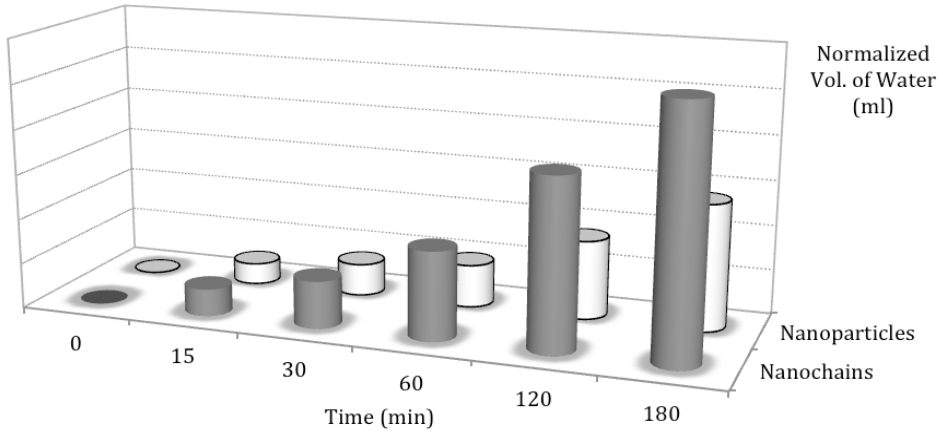

Figure 8. The volume of water collected through the filters with nanochains, and nanoparticles as adsorbent materials at different time points. The bar graph shows a higher flow rate with nanochain-based filters than with an equivalent mass of nanoparticles.

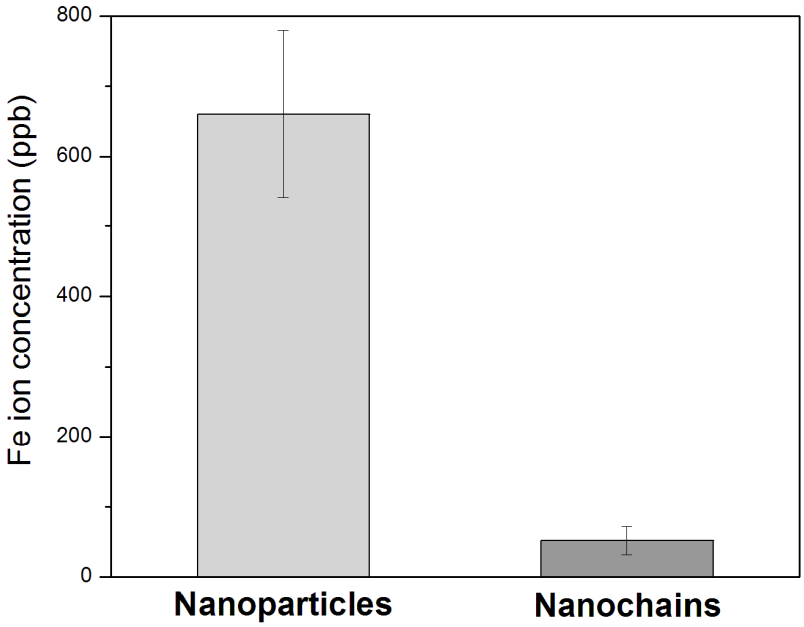

Figure 9. The Fe ions detected by ICP-MS in water that was filtered through nanoparticles and nanochains at a fixed flow rate and a fixed total time.

TABLE.

Table 1. Comparison of arsenic removal capacities of some iron based and commercial nanoadsorbent reported in the literature

Adsorbents	**S_{BET}** **(m^2 g^{-1})**	**Q_m** **(mg g^{-1})**	**Ref**
γ-Fe_2O_3 nanochains	151	162	This study
γ-Fe_2O_3 NPs	169	95.4	[46]
α-FeOOH	96.9	58	[47]
Chestnut-like Fe_2O_3	143	137	[48]
Fe_3O_4 nanoparticles	102	44.1	[49]
$MnFe_2O_4$ nanoparticles	138	90.4	[49]
Mesoporous Fe_2O_3@C	877	29.4	[5]
γ-Fe_2O_3 NPs in Mesoporous Silica	155	248	[4]
Bayoxide E33	158	12	[50]